

Effects of filling, strain, and electric field on the Néel vector in antiferromagnetic CrSb

In Jun Park,^{1,*} Sohee Kwon,¹ and Roger K. Lake^{1,†}

¹*Laboratory for Terascale and Terahertz Electronics (LATTE),
Department of Electrical and Computer Engineering,
University of California, Riverside, CA 92521, USA*

(Dated: February 12, 2022)

CrSb is a layered antiferromagnet (AFM) with perpendicular magnetic anisotropy, a high Néel temperature, and large spin-orbit coupling (SOC), which makes it interesting for AFM spintronic applications. To elucidate the various mechanisms of Néel vector control, the effects of strain, band filling, and electric field on the magnetic anisotropy energy (MAE) of bulk and thin-film CrSb are determined and analysed using density functional theory. The MAE of the bulk crystal is large (1.2 meV per unit cell). Due to the significant ionic nature of the Cr-Sb bond, finite slabs are strongly affected by end termination. Truncation of the bulk crystal to a thin film with one surface terminated with Cr and the other surface terminated with Sb breaks inversion symmetry, creates a large charge dipole and average electric field across the film, and breaks spin degeneracy, such that the thin film becomes a ferrimagnet. The MAE is reduced such that its sign can be switched with realistic strain, and the large SOC gives rise to an intrinsic voltage controlled magnetic anisotropy (VCMA). A slab terminated on both faces with Cr remains a compensated AFM, but with the compensation occurring nonlocally between mirror symmetric Cr pairs. In-plane alignment of the moments is preferred, the magnitude of the MAE remains large, similar to that of the bulk, and it is relatively insensitive to filling.

I. INTRODUCTION

Antiferromagnetic (AFM) materials are of great interest for future spintronics applications¹. Their resonant frequencies are much higher than those of ferromagnetic (FM) materials, which allows them to be used in the THz applications²⁻⁴ and ultrafast switching⁵. However, it is challenging to control and detect the antiferromagnetic states. There are several methods to control the spins in AFMs such as via exchange bias with a proximity FM layer⁶ and the use of electric current by Néel spin-orbit torque⁷. The latter method has been extensively studied, although the results have recently been questioned^{8,9}. Controlling the Néel vector without electric current is promising for ultra low power applications, since it has been predicted that magnetization reversal can be achieved with atto joule (aJ) level energy consumption¹⁰. Electric field control of the magnetic properties of AFMs can be realized indirectly through the mechanism of mechanical strain created from a piezoelectric substrate¹¹⁻¹⁷ or a combination of strain plus exchange spring¹⁸. It can also be realized directly through the mechanism of voltage controlled magnetic anisotropy (VCMA). This mechanism has been experimentally and theoretically studied for FMs¹⁹⁻⁴⁰, and the experimental results have been recently reviewed.⁴¹ Technological applications have been described and analysed⁴²⁻⁴⁴. More recently, several theoretical studies of VCMA in the AFM materials FeRh, MnPd, and MnPt have been reported^{5,45-47}.

CrSb crystallizes in the hexagonal NiAs-type structure, and the spins on the Cr atoms couple ferromagnetically within the hexagonal plane and antiferromagnetically along the hexagonal axis as shown in Fig. 1(a). In the ground state, the Néel vector aligns along the

hexagonal axis ([0001] direction), so that it has perpendicular magnetic anisotropy (PMA). The bands near the Fermi energy are composed of the d-orbitals of the Cr atoms, and these bands give rise to a large peak in the density of states near the Fermi energy.⁴⁸⁻⁵¹ The Sb atoms provide significant SOC. CrSb has a high Néel temperature (705 K) making it suitable for on-chip applications⁵². Recently, CrSb has been used to control the magnetic textures and tune the surface states of topological insulators⁵³⁻⁵⁵.

We examine three different physical mechanisms that alter the magnetic anisotropy of bulk and thin-film CrSb: (i) strain, (ii) electron filling, and (iii) electric field. Density functional theory (DFT) calculations of the magnetostriction coefficient, strain coefficient, filling coefficient, and VCMA coefficient characterize the effectiveness of the three methods in modifying the MAE.

II. METHODS

We perform first principles calculations as implemented in the Vienna Ab initio Simulation Package (VASP)⁵⁶ to investigate the effects of strain, electric field, and band filling on the magnetic anisotropy of CrSb. Projector augmented-wave (PAW) potentials⁵⁷ and the generalized gradient approximation (GGA) parameterized by Perdew-Burke-Ernzerhof (PBE) are employed⁵⁸. A cut-off energy of 500 eV and $8 \times 8 \times 8$ Γ -centered k-point grid were used to make sure the total energy converged within 10^{-7} eV per unit cell. A GGA+ U implementation was also used to reproduce the magnetic moment on the Cr atom corresponding to the experimental values⁵⁹. We used $U_{eff} = 0.25$ eV for the Cr atom where $U_{eff} = U - J$.

From the initial bulk structure, uniaxial strain along

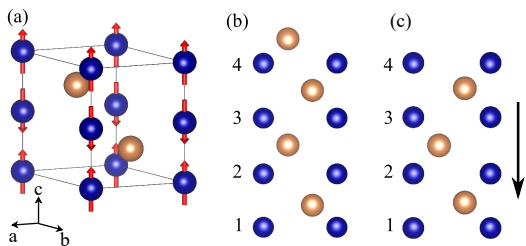


FIG. 1: (a) Bulk antiferromagnetic CrSb crystal structure and spin texture in the ground state. Blue and brown spheres indicate the Cr and Sb atoms, respectively. (b) 1.1 nm thin film with a thickness of 2 unit cells. (c) The same thin film as in (b) but with the top Sb layer removed. The numbers index the Cr atoms, and the arrow indicates the direction of positive applied external electric field for VCMA calculations.

the x -axis is applied and the structure is fully relaxed along y and z axes until all forces on each atom are less than 10^{-3} eV \AA^{-1} . Here, the x and z axes are parallel to the a and c lattice vectors of the hexagonal unit cell shown in the Fig. 1. The strain is defined as $\varepsilon = (a - a_0)/a_0 \times 100\%$ where a and a_0 are the lattice constants along x with and without strain, respectively. The calculated lattice constants without strain are $a_0 = 4.189$ \AA and $c_0 = 5.394$ \AA , which are close to those from experiment⁵⁹.

To obtain the charge density, a spin-polarized self-consistent calculation is performed with the relaxed structure for each strain. Using the obtained charge densities, E_{\parallel} and E_{\perp} , are calculated in the presence of SOC where E_{\parallel} and E_{\perp} are the total energies per unit cell with the Néel vector along [1000] and [0001] directions, respectively. The magnetic anisotropy energy (MAE) is defined as $E_{\text{MAE}} = E_{\parallel} - E_{\perp}$. For uniformity of comparison between bulk and thin-film structures, all values of E_{MAE} are reported per bulk unit cell (u.c.) (i.e. per two Cr atoms). For MAE calculations, a denser k-point grid ($16 \times 16 \times 16$) is used for accuracy. The same procedures are performed to investigate the effect of electron filling on the MAE, and the structures are optimized for each number of electrons in the unit cell.

Charge transfer between the Cr and Sb ions is analyzed by calculating both the Bader charges⁶⁰ and the planar averaged volumetric charge densities⁶¹. The “net electronic charge” on each atom is defined as the number of valence electrons for a given atom minus the Bader charge on the atom in units of $|e|$. Thus, a depletion of electrons is a positive electronic charge. The Bader charges are used to understand the effect of truncation of the bulk to a slab and the application of an electric field. For thin-films, the planar averaged volumetric charge densities at different electric fields are calculated by averaging the three-dimensional charge density over the $x-y$ plane for fixed positions z on the c axis.

To investigate the effect of strain and electric field on the MAE of thin-film CrSb, we consider slab struc-

tures consisting of 2 and 3 unit cells along the c -axis (~ 1.1 nm and 1.6 nm). A 15 \AA vacuum layer is included. The stability of two different surface terminations is quantified by calculating the cohesive energy defined as $E_{\text{coh}} = (E_{\text{crystal}} - E_{\text{isolated}})/N$ where N is the total number of atoms, E_{crystal} is the total energy of the relaxed slab structure, and E_{isolated} is the sum of the energies of the individual atoms. For the thin-film structures, a $23 \times 23 \times 1$ Γ -centered k-point grid with a 500 eV cutoff energy is used to ensure the same convergence criteria as the bulk structure. The structures are fully relaxed until all forces on each atom are less than 10^{-3} eV \AA^{-1} without changing the volume. Vertical external electric fields are applied to the slab by introducing a dipole layer in the middle of the vacuum layer. The dipole layer also corrects for the built in dipole moment in the CrSb slab structures to prevent interactions between the artificial periodic images^{62,63}. The equilibrium charge density is obtained by performing a spin-polarized self-consistent calculation without the electric field. Then, the charge densities with increasing applied electric fields along c -axis are obtained by relaxing the charges from the calculation with the previous electric field. For each electric field, the MAE is calculated using a $46 \times 46 \times 1$ k-point grid.

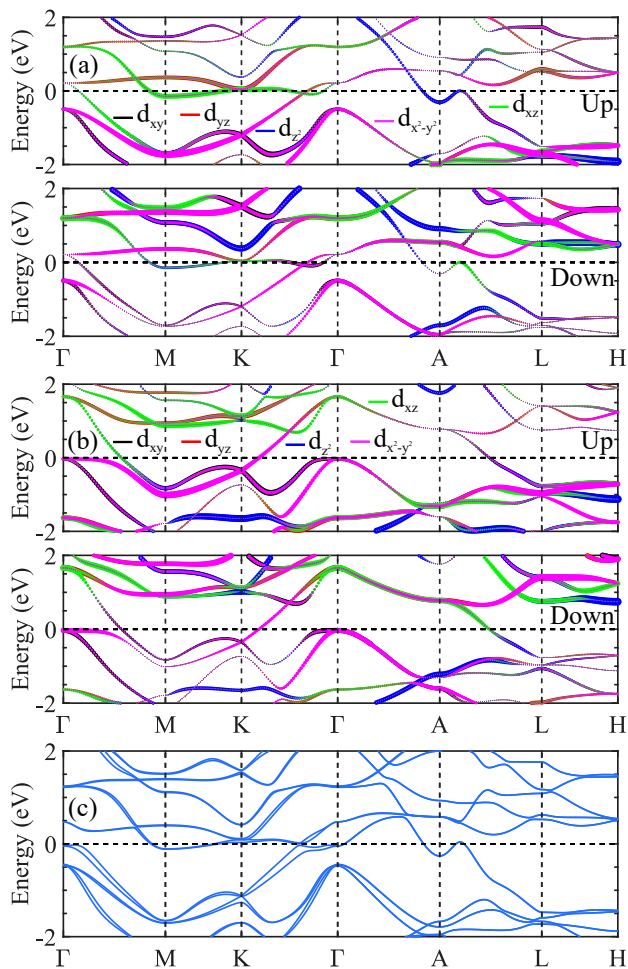


FIG. 2: The d-orbital resolved bandstructures (without SOC) of bulk CrSb when the electron number is (a) 22 (equilibrium) and (b) 21. For both (a) and (b), the top panel is for spin up, and the bottom panel is for spin down. The colors indicate the different d-orbitals, as indicated by the legends. The line thicknesses indicate the relative weights. (c) The bandstructure of CrSb in equilibrium with SOC.

III. RESULTS AND DISCUSSION

In Fig. 2, the electronic bandstructure of bulk CrSb is shown. Fig. 2(a) is the d-orbital resolved bandstructure for a Cr atom in equilibrium in the absence of SOC. The colors denote different orbitals as indicated by the legends, and the line thicknesses denote the relative occupations. The spin-up bands are shown in the top panel, and the spin-down bands are shown in the bottom panel. Fig. 2(c) shows the equilibrium bandstructure in the presence of SOC.

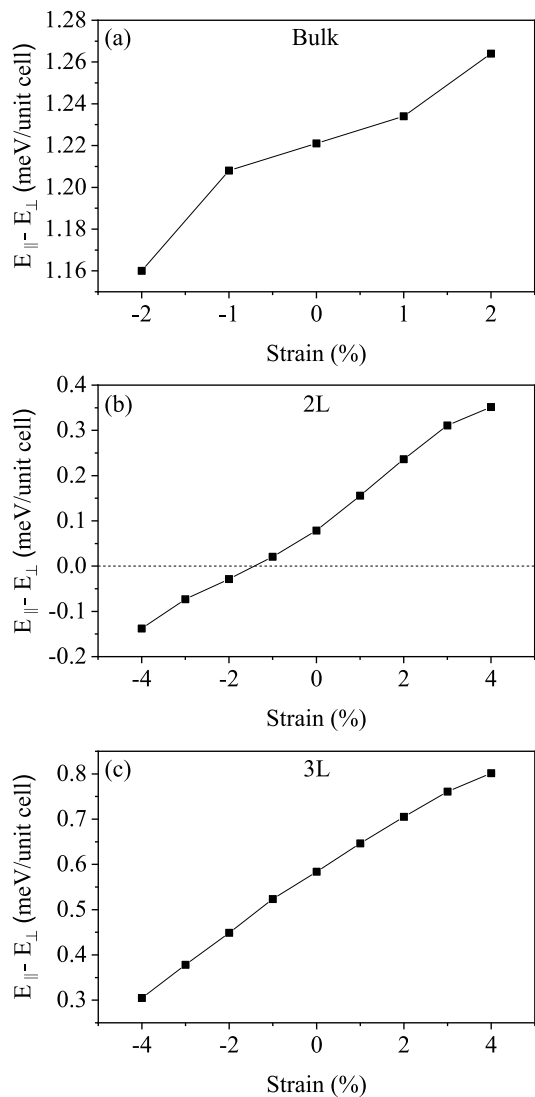


FIG. 3: MAE as a function of applied strain for (a) the bulk crystal and for the asymmetric (b) 1.1 nm and (c) 1.6 nm thin films.

The effect of spin-orbit coupling (SOC) on the bandstructure is relatively large. A comparison of Fig. 2(a) to 2(c) shows that the SOC breaks the spin degeneracy throughout much of the Brillouin zone and creates anti-crossings at a number of band-crossing points. The largest band splitting occurs at Γ . The two bands that touch at 0.2 eV in the absence of SOC are split by ~ 0.5 eV and the hole like band is pushed down below E_F .

Fig. 3(a) shows E_{MAE} plotted as a function of applied strain for bulk CrSb. The value at zero strain is $E_{MAE} = 1.2$ meV/u.c. The positive sign of the MAE means that the Néel vector aligns along the c-axis (out-of-plane) independent of the strain. The monotonic increase in the MAE indicates that CrSb behaves like a magnet with a negative magnetostriction coefficient, since the tensile strain favors out-of-plane anisotropy. The mag-

netostriction coefficient (λ_s) is defined as

$$\lambda_s(\text{ppm}) = -\frac{2K_{me}(1-v^2)}{3E\varepsilon}, \quad (1)$$

where v , E , and ε are the Poisson's ratio (0.288), Young's modulus (78.3 GPa), and strain, respectively⁶⁴. The magnetoelastic anisotropy constant, K_{me} , is calculated from the difference between two MAEs with and without strain (i.e., $E_{\text{MAE}}(\varepsilon) - E_{\text{MAE}}(0)$). The parameters v and E are taken from a previous study⁶⁵. The calculated λ_s for small strain (between -1% to 1%) is -19.8 ppm. CrSb has a negative value of λ_s , and the magnitude of λ_s is similar to that of MnNi and MnPd¹³. We also define a strain coefficient as $\alpha_\varepsilon = dE_{\text{MAE}}/d\varepsilon$ evaluated at $\varepsilon = 0$. The value for bulk CrSb is $\alpha_\varepsilon = 0.013$ meV/%strain.

The response of the bulk MAE as a function of the electron number in the unit cell is shown in Fig. 4. In equilibrium, the unit cell has 22 valence electrons, which is denoted by the vertical line in the figure. The MAE decreases most rapidly when the CrSb is depleted, and it changes sign when the hole doping reaches 0.75/u.c. For electron depletion, the filling coefficient, defined as $\alpha_n = dE_{\text{MAE}}/dn$, is 2.92 meV, where n is the electron number per unit cell.

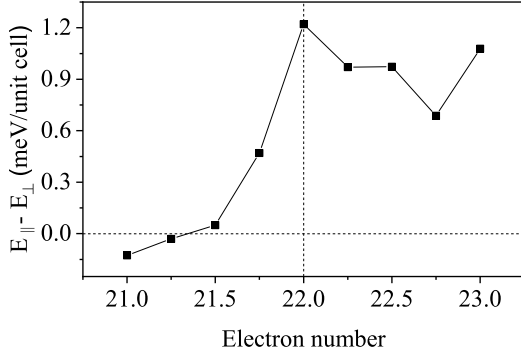


FIG. 4: MAE of bulk crystal versus the number of electrons in the unit cell.

To understand the physical origin of the transition due to charge depletion, we consider the d-orbital resolved band structures for a Cr atom plotted for 2 different electron numbers in the unit cell, 22 (equilibrium) in Fig. 2(a) and 21 in Fig. 2(b). Within second-order perturbation theory, the MAE is approximately expressed as⁶⁶

$$\begin{aligned} MAE \propto & \xi^2 \sum_{o,u} \frac{|\langle \Psi_o^\uparrow | \hat{L}_z | \Psi_u^\uparrow \rangle|^2 - |\langle \Psi_o^\uparrow | \hat{L}_{x(y)} | \Psi_u^\uparrow \rangle|^2}{E_u^\uparrow - E_o^\uparrow} \\ & + \xi^2 \sum_{o,u} \frac{|\langle \Psi_o^\downarrow | \hat{L}_z | \Psi_u^\downarrow \rangle|^2 - |\langle \Psi_o^\downarrow | \hat{L}_{x(y)} | \Psi_u^\downarrow \rangle|^2}{E_u^\downarrow - E_o^\downarrow} \\ & + \xi^2 \sum_{o,u} \frac{|\langle \Psi_o^\uparrow | \hat{L}_{x(y)} | \Psi_u^\downarrow \rangle|^2 - |\langle \Psi_o^\uparrow | \hat{L}_z | \Psi_u^\downarrow \rangle|^2}{E_u^\downarrow - E_o^\uparrow}, \end{aligned} \quad (2)$$

where $(\Psi_u)\Psi_o$, $(E_u)E_o$, and ξ are the (un)occupied states, (un)occupied eigenvalues, and the spin-orbit

coupling constant, respectively. \hat{L}_z and $\hat{L}_{x(y)}$ are the out-of plane and in-plane components of the orbital angular momentum operator, and \uparrow and \downarrow denote spin-up and spin-down. The non-zero matrix elements in the Eq. (2) are $\langle d_{xz} | \hat{L}_z | d_{yz} \rangle$, $\langle d_{x^2-y^2} | \hat{L}_z | d_{xy} \rangle$, $\langle d_{z^2} | \hat{L}_x | d_{yz} \rangle$, $\langle d_{xy} | \hat{L}_x | d_{xz} \rangle$, $\langle d_{x^2-y^2} | \hat{L}_x | d_{yz} \rangle$, $\langle d_{z^2} | \hat{L}_y | d_{xz} \rangle$, $\langle d_{xy} | \hat{L}_y | d_{yz} \rangle$, and $\langle d_{x^2-y^2} | \hat{L}_y | d_{xz} \rangle$. The largest contributions to Eq. (2) come from pairs of nearly degenerate occupied and unoccupied states near the Fermi level. In equilibrium (Fig. 2(a)), the main contributions to the MAE come from the spin-orbit coupling between occupied d_{xz}^\uparrow and unoccupied d_{yz}^\uparrow states at the K point and near the Γ point, and between occupied d_{xy}^\downarrow and unoccupied $d_{x^2-y^2}^\downarrow$ states near the Γ point. All of these states couple through the \hat{L}_z operator, which results in the positive MAE value (out-of-plane anisotropy). When CrSb is depleted (see Fig. 2(b)), the entire band structure moves upward so that the main contributor states of the perpendicular anisotropy become unoccupied. This reduces the value of the MAE, and eventually reverses the sign for $n = 21.25$.

Below, we will compare the sensitivity of the bulk crystal MAE to electron filling with the sensitivity of the thin-film MAE to applied electric field. Such a comparison requires a common metric based on a common physical quantity that governs the MAE. Assuming that the common driving mechanism is the population change of the magnetic Cr atoms³¹, we determine a slightly different parameter,

$$\alpha_{\bar{n}_{\text{Cr}}} = dE_{\text{MAE}}/d\bar{n}_{\text{Cr}}, \quad (3)$$

where \bar{n}_{Cr} is the average electron number on the Cr atoms as determined from the Bader charges. Due to the strongly ionic nature of the Cr-Sb bond, only $\sim 1/3$ of the hole doping goes to the Cr sublattice. The equilibrium charge resulting from a transfer of ~ 0.7 electrons from the Cr atom to the Sb atom is shown in Fig. 5(a), and the change in charge at a filling of -0.5 electrons / u.c. is shown in Fig. 5(b). The filling of -0.5 electrons / u.c. corresponds to -0.07 electrons / Cr atom. Using the values from Fig. 5(b), for hole doping, $\alpha_{\bar{n}_{\text{Cr}}} = 16.2$ meV.

We now consider thin-film slabs with thicknesses of 2 and 3 unit cells corresponding to 1.1 nm and 1.6 nm, respectively. For the thinner slab, the cohesive energies are calculated for a 7 atomic layer structure of alternating Cr and Sb layers terminated on both ends with a Cr layer and for a 8 atomic layer structure (2 unit cells) terminated on one end with Cr and on the other with Sb. The cohesive energies of the 7 and 8 atomic layer structures are -3.328 eV and -3.517 eV, respectively. For the thicker slab, cohesive energies are calculated for an 11 atomic layer structure and a 12 atomic layer structure, and the cohesive energies are -3.522 eV and -3.636 eV, respectively. Thus, the slab structures with an integer number of unit cells such that one face is a Cr layer and the opposing face is an Sb layer are the most stable, and they are the ones that we will consider first. We will refer

to these structures as asymmetric slabs.

In these asymmetric slabs, inversion symmetry is broken, since one end is terminated with a Cr layer and the other end is terminated with a Sb layer. Thus, these thin films are also Janus structures. The two unit cell asymmetric thin-film is shown in Fig. 1(b). Below, results for strain and VCMA coefficients are presented for both the 2 and 3 unit cell asymmetric thin-films, and the in-depth microscopic analysis of the charge, magnetic moments, and electronic structure focuses on the 2 unit cell asymmetric thin-film.

In the asymmetric thin films, there is a net polarization of electron charge between the positively charged Cr layer on the bottom and the negatively charged Sb layer on the top. The excess charges on each atom, as determined from the Bader charges, in the bulk and in the 2 unit-cell slab are shown in Fig. 5(a,c), and it is clear that, in the slab, the charge transfer is no longer balanced layer-by-layer. The net charge polarization gives rise to a built-in electric field that alternates positively and negatively within the slab, but, its average value points from the positive Cr layer on the bottom to the negative Sb layer on the top. This built-in electric field results in a built-in potential across the slab of 1.7 eV as shown by the plot of the equilibrium planar averaged Hartree potential in Fig. 5(d).

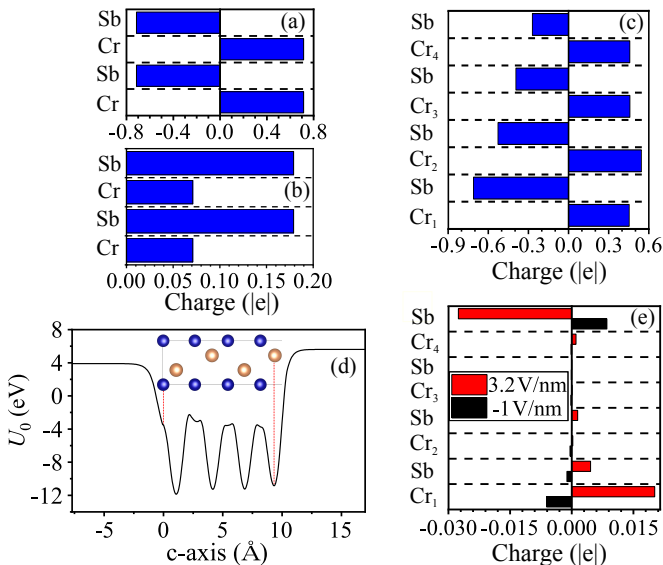


FIG. 5: The net electronic charges on the Cr and Sb atoms, calculated from the Bader charges, in units of $|e|$, of (a) bulk and (c) 1.1 nm thin film CrSb in equilibrium. (b) Change in net electronic bulk charge due to hole doping of 0.5 holes / unit cell. (d) The planar-averaged Hartree potential of the 1.1 nm thin film CrSb in equilibrium. (e) Change in the net electronic charges induced by the electric field (indicated in the legend) with the reference charge taken from equilibrium charges shown in (c). Note that a net positive electronic charge corresponds to a depletion of the electron density.

The truncation of the bulk to a finite slab results not only in a loss of *local* balance between the positive and

negative charges, but also in a *global* imbalance of the magnetic moments of the Cr ions. In other words, the cancellation of magnetic moments between alternating layers of Cr is no longer exact, and a small net magnetic moment exists in the slab. The magnetic moments on each Cr atom are listed in the ‘ $\mu_{Cr,Sb}$ ’ column of Table I with the numbering of the Cr atoms corresponding to that shown in Fig. 1(b). The magnitudes of the magnetic moments in the Cr layers monotonically decrease from bottom to top as the Cr atoms approach the Sb terminated end of the slab. The breaking of the spin degeneracy is readily apparent in the bandstructure of the slab shown in Fig. 6(a). The degeneracy between the up-spin and down-spin bands is broken, and the CrSb slab has become a ferrimagnet (FiM). The breaking of the spin degeneracy of the AFM states in a finite slab of a layered AFM is explained by a simple chain model with different end terminations described in [67]. The wavefunctions of a pair of degenerate AFM states are weighted differently on alternate atoms of the magnetic lattice. Thus, the coupling of the two states to an end atom is different, and this different coupling breaks the degeneracy of the two states.

TABLE I: Magnetic moment, in units of μ_B , for each Cr atom in the bulk and thin films of Fig. 1 with spin-orbit coupling. The indices on the Cr atoms correspond to those in Fig. 1. $\mu_{Cr,Sb}$ corresponds to the thin film of Fig. 1(b) with an integer number of unit cells, and $\mu_{Cr,Cr}$ corresponds to the thin film of Fig. 1(c) in which the top Sb layer is removed.

Atom	μ_{bulk}	$\mu_{Cr,Sb}$	$\mu_{Cr,Cr}$
Cr ₁	3.035	3.763	3.905
Cr ₂	-3.035	-3.190	-2.994
Cr ₃		3.116.	2.994
Cr ₄		-2.889.	-3.904

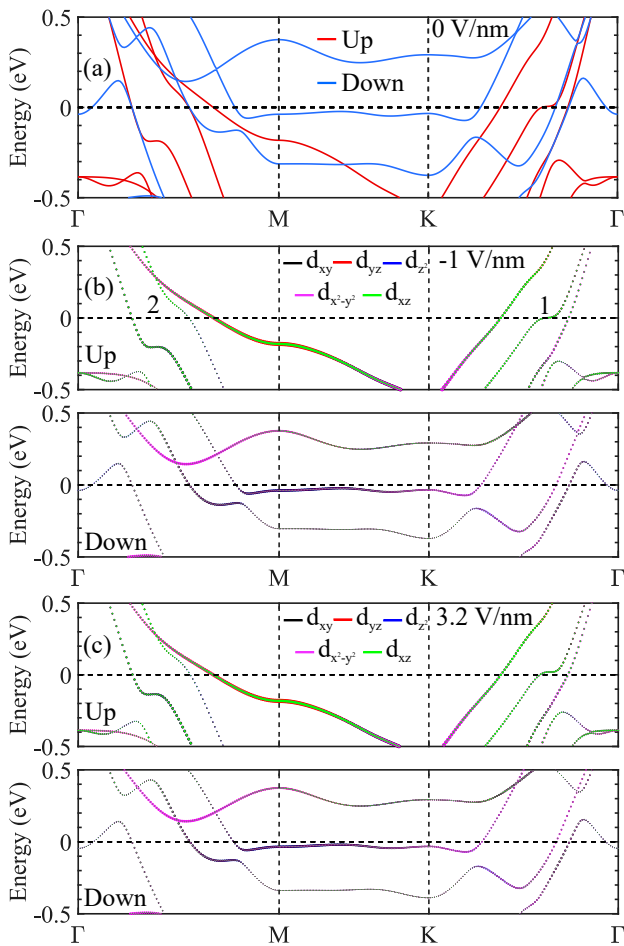


FIG. 6: (a) Spin resolved bandstructure of the 1.1 nm CrSb thin-film in equilibrium. (b,c) The d-orbital resolved bandstructures of the 1.1 nm CrSb thin-film under electric fields of (b) -1 V/nm and (c) 3.2 V/nm. The line colors indicate the d-orbital composition as given by the legends, and the line thicknesses indicate the relative weights.

A third result of truncating the bulk to a slab is that the MAE decreases. For the 1.1 nm slab, the MAE is reduced by a factor of 15 from 1.2 meV/u.c. to 0.079 meV/u.c. (0.17 erg/cm²), and for the 1.6 nm slab, the MAE is reduced by a factor of 2.1 to 0.58 meV/u.c. (1.85 erg/cm²). Also, the sensitivity of the MAE to strain increases. The strain coefficients of the 1.1 and 1.6 nm slabs (α_ε) increase from 0.013 meV/%strain in the bulk to 0.068 meV/%strain and 0.062 meV/%strain, respectively, where the energies are per bulk unit cell (2 Cr atoms). The combined result of the reduced MAE and increased strain coefficient is that a 1.5% uniaxial compressive strain along [1000] direction in the 1.1 nm thin film causes a 90° rotation of the Néel vector from out-of-plane to in-plane as shown in Fig. 3(b).

A fourth result is that the MAE also becomes sensitive to an external electric field as shown in Fig. 7. In other words, the thin slab exhibits intrinsic VCMA. Typically VCMA is found when a magnetic layer is placed in contact with a heavy-metal layer that provides SOC.

However, the Sb layers provide large SOC, and the terminating Sb layer serves as the HM layer, such that the CrSb slab has intrinsic VCMA. The MAE decreases linearly as the electric field is increased, and, for the 1.1 nm slab, it changes sign at 3.2 V/nm, which indicates that the Néel vector rotates 90° from out-of-plane to in-plane.

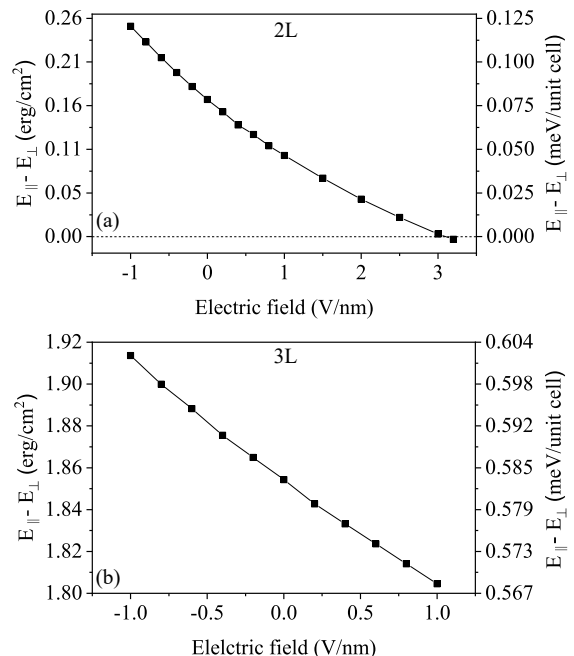


FIG. 7: MAEs of (a) 1.1 nm and (b) 1.6 nm films as a function of applied electric field.

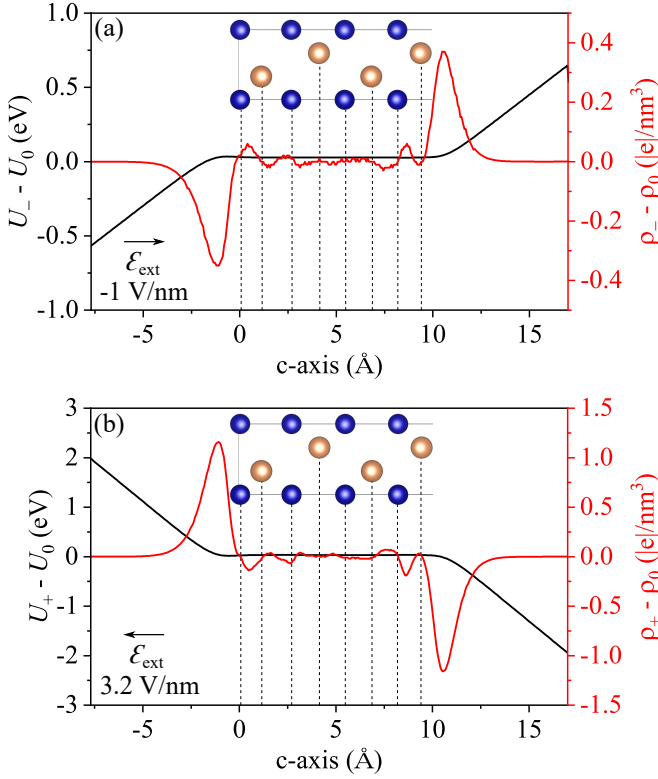


FIG. 8: The change in the planar-averaged electronic charge (red) and planar-averaged Hartree energy (black) of 1.1 nm thin film CrSb with an electric field of (a) -1 V/nm and (b) 3.2 V/nm. The arrow indicates the direction of applied electric field. Note that a positive electronic charge corresponds to a depletion of the electron density.

The standard metric describing the sensitivity of the MAE to the applied electric field is given by the VCMA coefficient defined as

$$\beta = \frac{dE_{\text{MAE}}^s}{d\mathcal{E}_I} = \frac{dE_{\text{MAE}}^s}{d\mathcal{E}_{\text{ext}}/\epsilon_I}, \quad (4)$$

where E_{MAE}^s is the MAE per unit area of the slab, \mathcal{E}_{ext} is the external electric field and \mathcal{E}_I and ϵ_I are the electric field and the relative dielectric constant in the insulator, respectively. In a typical experiment, the insulator would be an oxide layer with $\epsilon_I > 1$. In our case, the insulator is the vacuum, so that $\epsilon_I = 1$ and $\mathcal{E}_I = \mathcal{E}_{\text{ext}}$. The values of β , evaluated at $\mathcal{E}_{\text{ext}} = 0$ V/nm, are -76.4 fJV⁻¹m⁻¹ for the 1.1 nm film and -55.3 fJV⁻¹m⁻¹ for the 1.6 nm slab.

The calculated magnitudes of β are comparable with many of the experimentally measured values of β from heavy metal/FM/MgO heterostructures,^{24,26-28,30,32,34,35} with magnitudes ranging from 65 fJV⁻¹m⁻¹ in a Ta/Co_{0.25}Fe_{0.55}B_{0.20}/MgO structure³⁰ to 139 fJV⁻¹m⁻¹ in a Ru/Co₂FeAl/MgO structure.³² However, they are considerably smaller than the values of 370 fJV⁻¹m⁻¹ and 1043 fJV⁻¹m⁻¹ measured in Cr/Fe/MgO and Ir/CoFeB/MgO structures, respectively.^{33,36} A lengthy table of experimental values

compiled from the literature is provided in a recent review⁴¹. Theoretical studies of AFM materials have calculated magnitudes of β both larger and smaller than the values for CrSb. For a G-AFM FeRh/MgO bilayer, the magnitude of β was in the range of 130 to 360 fJV⁻¹m⁻¹ depending on the sign of the electric field, the strain, and the termination layer of either Fe or Rh⁴⁵. A value of 22.6 fJV⁻¹m⁻¹ was calculated for Pt/MnPd with vacuum as the dielectric⁴⁶. VCMA calculations of a MgO/MnPt/MgO slab found magnitudes of 170 fJV⁻¹m⁻¹ and 70 fJV⁻¹m⁻¹ depending on whether the MnPt layer was terminated on both ends with either Mn or Pt, respectively⁴⁷.

To understand which Cr atoms contribute to the VCMA effect, we inspect the change in charge of the Cr atoms in response to the applied field. The change in charge with applied electric field, plotted in Figs. 5(e) and 8, shows that, among the Cr atoms, the only significant change in charge occurs on Cr₁. This is to be expected, since the electric field is screened by the first and last atomic layers from the interior of the CrSb metal. The first atomic layer is Cr and the last is Sb, so that an applied field creates a net change in charge on the Cr sublattice with the charge being transferred to the Sb sublattice.

The sensitivities of the MAE of the thin film slabs to the average charging of the Cr atoms due to an applied electric field is comparable to the sensitivity of the bulk MAE to the filling of the Cr atoms. The values of $\alpha_{\bar{n}_{\text{Cr}}}$ evaluated at $\mathcal{E}_{\text{ext}} = 0$ are 19.7 meV and 13.9 meV for the 2 layer and 3 layer slabs, respectively. For comparison, the bulk value for hole doping is $\alpha_{\bar{n}_{\text{Cr}}} = 16.2$ meV. Thus, the sensitivity of the MAE per unit cell to the change in the average charge on the Cr atoms lies in the range of 13 - 20 meV for both of the slabs and the bulk.

To elucidate the physical origin of switching mechanism in the two layer slab, the d-orbital resolved band structures for the Cr₁ atom under different electric fields are plotted in Fig. 6(b,c). At the electric field of -1 V/nm, the major contribution of the perpendicular anisotropy comes from the spin-orbit coupling between the unoccupied d_{xz}^{\uparrow} and occupied $d_{x^2-y^2}^{\downarrow}$ states through \hat{L}_y operator in the region 1. Although the states in the region 1 are coupled through the in-plane angular momentum operator, the contribution of the MAE is positive since they are from different spin channels. In the region 2, the occupied d_{xy}^{\uparrow} states are coupled with unoccupied d_{xz}^{\uparrow} states through \hat{L}_x , which contributes the in-plane anisotropy. As the external field increases (see Fig. 6(c)), the unoccupied d_{xz}^{\uparrow} states in the region 1 move away from the Fermi level by 18 meV, which results in the reduction of the out-of-plane anisotropy, since the denominator in the Eq. 2 increases. In addition, in the region 2, the occupied d_{xy}^{\uparrow} states move closer to the Fermi energy by 67 meV as the electric field increases so that the in-plane anisotropy increases.

Previous studies have shown that the choice of surface

termination of a FM layer can alter, or even change the sign of the MAE^{45,47,68,69}. Thin film CrSb is no exception. The final structure that we consider is the slab shown in Fig. 1(c). It is identical to the 1.1 nm thin film analyzed above, except that the top Sb layer is removed so that the thin film becomes mirror symmetric with respect to the $x - y$ plane. As a result, there is no net electrical dipole moment or built-in potential across the slab. The net magnetic moment of the slab remains zero, as shown in the last column of Table I. The magnetic moment is no longer compensated locally in each unit cell; the compensation occurs between the mirror symmetric pairs of Cr atoms. Furthermore, the magnitude of the MAE (-1.07 meV / u.c) is more than an order of magnitude larger compared to that of the asymmetric slab (0.079 meV / u.c), and it changes sign, so that in-plane alignment of the magnetic moments is preferred. The magnitude of the MAE is similar to that of the bulk (1.2 meV / u.c), but with opposite sign. Note that the value of -1.07 meV / u.c. is obtained by taking the total MAE of the slab and dividing by two, since it contains two unit cells of magnetic ions even though the last Sb layer of the top unit cell is missing.

Applying an electric field to this symmetric slab depletes electrons from the bottom Cr layer and accumulates electrons on the top Cr layer, so that the net change in charge on the Cr layers is zero. This is in contrast to the effect of an electric field on the antisymmetric slab where the applied field depletes electrons from the bottom Cr layer and accumulates electrons on the top Sb layer, with the overall effect being a net depletion of electrons on the Cr atoms. In the symmetric slab, with no net change in charge on the Cr atoms, the MAE remains unchanged to 4 significant digits over the range of $-1 \leq \mathcal{E}_{\text{ext}} \leq 3$ V/nm. This is consistent with results of prior simulations of symmetric MgO / FM / MgO and MgO / AFM / MgO structures^{19,47}.

To estimate the sensitivity of the MAE of the symmetric slab to electron filling, we alter the electron number of the slab by applying a compensating background charge, as we did in the bulk. Since the background charge is uniformly distributed throughout the simulation domain, which includes the vacuum region, the majority of the compensating charge in the CrSb slab is located on the outer two Cr layers. Depleting 0.5 electrons from the CrSb slab results in a total reduction of 0.32 electrons from the Cr sublattice with an average reduction of 0.080 electrons from the Cr atoms. The MAE changes from -1.07 meV to -0.7 meV, so that $\alpha_{\bar{n}_{\text{Cr}}} = -4.6$ meV. The negative sign means that as electrons are removed, the in-plane orientation of the Néel vector becomes less stable. The magnitude of $\alpha_{\bar{n}_{\text{Cr}}}$ is a factor of 4 less than that of the asymmetric slab, and the sign is opposite. Thus, the mirror symmetric slab of just 4 Cr layers has a high in-plane MAE, similar in magnitude to that of the bulk, and it is relatively insensitive to filling. Physically realizing such a structure would be challenging.

In a typical physical structure, the CrSb slab will be

sandwiched between a MgO layer on one face and a grounded heavy-metal (HM) layer on the opposing face. The electric field in the dielectric MgO will terminate at the CrSb where it will accumulate or deplete charge on the first atomic layer of the CrSb as shown at the left of Fig. 8. In the physical structure, there is no corresponding charge depletion or accumulation on the opposing face of the CrSb slab, since the HM is grounded and supplies the charge required to screen the electric field at the MgO/CrSb interface. Also, there will naturally be asymmetry and a built in potential across the CrSb slab due to the proximity of MgO on one face and a HM on the other. Since breaking the mirror symmetry of the slab breaks the degeneracy of the AFM states, it is most probable that the CrSb in a MgO/CrSb/HM structure will be in a FiM state. For the electric field in the MgO to significantly alter the charge on the Cr sublattice, the CrSb should be terminated with a Cr layer at the MgO interface.

Finally, we note that the parameter $\alpha_{\bar{n}_{\text{Cr}}}$, which gives the sensitivity of the MAE to the magnetic sublattice filling, is simply related to the conventional VCMA parameter β by

$$\alpha_{\bar{n}_{\text{Cr}}} \approx -\frac{2|e|}{\epsilon}\beta, \quad (5)$$

where $\epsilon = \epsilon_0\epsilon_I$, is the dielectric constant of the insulator, and the the negative sign is consistent with the sign of the positive electric field and the orientation of the slab in Fig. 1. The sign would reverse if either the field or the slab were reversed. Equation (5) is derived by noting that the induced charge lies primarily on Cr_1 , and, therefore, it can be approximated as a sheet density of an ideal metal given by $n_s = n_{\text{Cr}_1}/A_{u.c.} \approx \bar{n}_{\text{Cr}}N_L^{\text{Cr}}/A_{u.c.} \approx -\epsilon\mathcal{E}$ where $A_{u.c.}$ is the area of the unit cell in the basal plane, and N_L^{Cr} is the number of Cr layers in the slab. Also, $E_{\text{MAE}}^s = E_{\text{MAE}}N_{u.c.}/A_{u.c.}$ where $N_{u.c.} = N_L^{\text{Cr}}/2$. With these relations, we can write, $dE_{\text{MAE}}/d\bar{n}_{\text{Cr}} \approx -\frac{2|e|}{\epsilon}dE_{\text{MAE}}^s/d\mathcal{E}$, which is Eq. (5). This expression slightly underestimates the magnitude of $\alpha_{\bar{n}_{\text{Cr}}}$, since the screening is not ideal. For example, in the asymmetric 2-layer slab, $\beta = -76.4$ fJv⁻¹m⁻¹. Using this value in Eq. (5), gives $\alpha_{\bar{n}_{\text{Cr}}} = 17.3$ meV, whereas the actual value is $\alpha_{\bar{n}_{\text{Cr}}} = 19.7$ meV. This relationship between $\alpha_{\bar{n}_{\text{Cr}}}$ and β assumes that the slab terminates with a magnetic layer adjacent to the dielectric, and the one term specific to CrSb comes from the ratio $N_L^{\text{Cr}}/N_{u.c.}$ that was explicitly evaluated to give the factor of 2 in Eq. (5). This provides a simple relationship between the conventional metric β and the sensitivity of the MAE to the underlying driving mechanism of sublattice filling.

IV. SUMMARY AND CONCLUSIONS

The effects of strain, band filling, and electric field on the MAE of bulk and thin-film CrSb are determined and

analysed. A new metric that describes the sensitivity of the MAE to the filling of the magnetic sublattice provides a means to compare the effects of electric field and band filling on the MAE. The magnitude of the bulk magnetostriction coefficient is comparable with those from other antiferromagnets and ferromagnets, however the MAE is large (1.2 meV/u.c.) and its sign cannot be changed by strain for bulk material. For bulk CrSb, depleting the electron density by 0.75 electrons per unit cell depletes the flat, nearly-degenerate d-orbital bands near the Fermi energy and causes a 90° rotation of the Néel vector from out-of-plane to in-plane. Due to the significant ionic nature of the Cr-Sb bond, finite slabs are strongly affected by end termination. Truncation of the bulk crystal to a thin film consisting of an even number of unit cells, such that one face is a Cr layer and the opposing face is an Sb layer, breaks inversion symmetry, creates a large charge dipole and potential difference across the slab, and breaks spin degeneracy such that the CrSb slab becomes a ferrimagnet. For the 1.1 nm (1.6 nm) slab, the MAE is reduced from 1.2 meV/u.c. to 0.079 meV/u.c. (0.58 meV/u.c) and the strain coefficient is increased from 0.013 meV/%strain to 0.068 meV/%strain (0.062 meV/%strain). As a result of the reduced MAE and increased strain coefficient, the sign of the MAE in the 1.1 nm slab can be switched with 1.5% uniaxial com-

pressive strain. The large SOC from the Sb combined with broken inversion symmetry of the thin film results in an intrinsic VCMA. The calculated VCMA coefficients for the free-standing 1.1 nm and 1.6 nm thin films with vacuum as the insulator are $-76.8 \text{ fJv}^{-1}\text{m}^{-1}$ and $-55.6 \text{ fJv}^{-1}\text{m}^{-1}$, respectively. If the CrSb slab is terminated with Cr layers on both faces, then it remains a compensated AFM, but with the compensation occurring non-locally between mirror symmetric Cr pairs. The MAE changes sign so that in-plane alignment of the moments is preferred, the magnitude of the MAE remains large similar to that of the bulk, and it is relatively insensitive to filling. Finally, in a standard experimental configuration, the CrSb slab will have different end terminations with MgO on one face and a HM on the other, so that the FiM state of the asymmetric slab will be the most probable one observed experimentally.

Acknowledgements: This work was supported as part of Spins and Heat in Nanoscale Electronic Systems (SHINES) an Energy Frontier Research Center funded by the U.S. Department of Energy, Office of Science, Basic Energy Sciences under Award DE-SC0012670. This work used the Extreme Science and Engineering Discovery Environment (XSEDE)⁷⁰, which is supported by National Science Foundation Grant No. ACI-1548562 and allocation ID TG-DMR130081.

* ipark008@ucr.edu

† rlake@ece.ucr.edu

- ¹ V. Baltz, A. Manchon, M. Tsoi, T. Moriyama, T. Ono, and Y. Tserkovnyak, *Rev. Mod. Phys.* **90**, 015005 (2018).
- ² T. Jungwirth, X. Marti, P. Wadley, and J. Wunderlich, *Nature Nanotechnology* **11**, 231 (2016).
- ³ E. V. Gomonay and V. M. Loktev, *Low Temperature Physics* **40**, 17 (2014).
- ⁴ F. Keffer and C. Kittel, *Physical Review* **85**, 329 (1952).
- ⁵ V. Lopez-Dominguez, H. Almasi, and P. K. Amiri, *Physical Review Applied* **11**, 024019 (2019).
- ⁶ J. Nogués and I. K. Schuller, *Journal of Magnetism and Magnetic Materials* **192**, 203 (1999).
- ⁷ P. Wadley, B. Howells, J. Železný, C. Andrews, V. Hills, R. P. Campion, V. Novák, K. Olejník, F. Maccherozzi, S. S. Dhesi, *et al.*, *Science* **351**, 587 (2016).
- ⁸ C. C. Chiang, S. Y. Huang, D. Qu, P. H. Wu, and C. L. Chien, *Phys. Rev. Lett.* **123**, 227203 (2019).
- ⁹ A. Churikova, D. Bono, B. Neltner, A. Wittmann, L. Scipioni, A. Shepard, T. Newhouse-Illige, J. Greer, and G. S. D. Beach, *Applied Physics Letters* **116**, 022410 (2020).
- ¹⁰ Y. G. Semenov, X.-L. Li, and K. W. Kim, *Physical Review B* **95**, 014434 (2017).
- ¹¹ A. Barra, J. Domann, K. W. Kim, and G. Carman, *Physical Review Applied* **9**, 034017 (2018).
- ¹² H. Yan, Z. Feng, S. Shang, X. Wang, Z. Hu, J. Wang, Z. Zhu, H. Wang, Z. Chen, H. Hua, *et al.*, *Nature Nanotechnology* **14**, 131 (2019).
- ¹³ I. J. Park, T. Lee, P. Das, B. Debnath, G. P. Carman, and R. K. Lake, *Applied Physics Letters* **114**, 142403 (2019).

- ¹⁴ X. Chen, X. Zhou, R. Cheng, C. Song, J. Zhang, Y. Wu, Y. Ba, H. Li, Y. Sun, Y. You, *et al.*, *Nature materials* **18**, 931 (2019).
- ¹⁵ X. Wang, Z. Feng, P. Qin, H. Yan, X. Zhou, H. Guo, Z. Leng, W. Chen, Q. Jia, Z. Hu, *et al.*, *Acta Materialia* **181**, 537 (2019).
- ¹⁶ D. Boldrin, A. P. Mihai, B. Zou, J. Zemen, R. Thompson, E. Ware, B. V. Neamtu, L. Ghivelder, B. Esser, D. W. McComb, *et al.*, *ACS applied materials & interfaces* **10**, 18863 (2018).
- ¹⁷ Z. Liu, H. Chen, J. Wang, J. Liu, K. Wang, Z. Feng, H. Yan, X. Wang, C. Jiang, J. Coey, *et al.*, *Nature Electronics* **1**, 172 (2018).
- ¹⁸ C. Feng, Y. Li, L. Wang, Y. Cao, M. Yao, F. Meng, F. Yang, B. Li, K. Wang, and G. Yu, *Advanced Functional Materials* **30**, 1909708 (2020).
- ¹⁹ C.-G. Duan, J. P. Velev, R. F. Sabirianov, Z. Zhu, J. Chu, S. S. Jaswal, and E. Y. Tsymbal, *Phys. Rev. Lett.* **101**, 137201 (2008).
- ²⁰ K. Nakamura, R. Shimabukuro, Y. Fujiwara, T. Akiyama, T. Ito, and A. J. Freeman, *Phys. Rev. Lett.* **102**, 187201 (2009).
- ²¹ M. K. Niranjan, C.-G. Duan, S. S. Jaswal, and E. Y. Tsymbal, *Applied Physics Letters* **96**, 222504 (2010).
- ²² P. K. Amiri and K. L. Wang, in *Spin*, Vol. 2 (World Scientific, 2012) p. 1240002.
- ²³ J. G. Alzate, P. Khalili Amiri, G. Yu, P. Upadhyaya, J. A. Katine, J. Langer, B. Ocker, I. N. Krivorotov, and K. L. Wang, *Applied physics letters* **104**, 112410 (2014).
- ²⁴ T. Nozaki, H. Arai, K. Yakushiji, S. Tamaru, H. Kub-

- ota, H. Imamura, A. Fukushima, and S. Yuasa, *Applied Physics Express* **7**, 073002 (2014).
- ²⁵ P. V. Ong, N. Kioussis, D. Odkhuu, P. Khalili Amiri, K. L. Wang, and G. P. Carman, *Phys. Rev. B* **92**, 020407 (2015).
- ²⁶ W. Skowroński, T. Nozaki, D. D. Lam, Y. Shiota, K. Yakushiji, H. Kubota, A. Fukushima, S. Yuasa, and Y. Suzuki, *Physical Review B* **91**, 184410 (2015).
- ²⁷ W. Skowroński, T. Nozaki, Y. Shiota, S. Tamaru, K. Yakushiji, H. Kubota, A. Fukushima, S. Yuasa, and Y. Suzuki, *Applied Physics Express* **8**, 053003 (2015).
- ²⁸ Y. Hibino, T. Koyama, A. Obinata, K. Miwa, S. Ono, and D. Chiba, *Applied Physics Express* **8**, 113002 (2015).
- ²⁹ T. Nozaki, A. Koziol-Rachwał, W. Skowroński, V. Zayets, Y. Shiota, S. Tamaru, H. Kubota, A. Fukushima, S. Yuasa, and Y. Suzuki, *Phys. Rev. Applied* **5**, 044006 (2016).
- ³⁰ Y. Shiota, T. Nozaki, S. Tamaru, K. Yakushiji, H. Kubota, A. Fukushima, S. Yuasa, and Y. Suzuki, *Applied Physics Letters* **111**, 022408 (2017).
- ³¹ J. Zhang, P. V. Lukashev, S. S. Jaswal, and E. Y. Tsymbal, *Phys. Rev. B* **96**, 014435 (2017).
- ³² Z. Wen, H. Sukegawa, T. Seki, T. Kubota, K. Takahashi, and S. Mitani, *Scientific reports* **7**, 45026 (2017).
- ³³ A. Koziol-Rachwał, T. Nozaki, K. Freindl, J. Korecki, S. Yuasa, and Y. Suzuki, *Scientific Reports* **7**, 5993 (2017).
- ³⁴ T. Kawabe, K. Yoshikawa, M. Tsujikawa, T. Tsukahara, K. Nawaoka, Y. Kotani, K. Toyoki, M. Goto, M. Suzuki, T. Nakamura, *et al.*, *Physical Review B* **96**, 220412 (2017).
- ³⁵ X. Li, K. Fitzell, D. Wu, C. T. Karaba, A. Buditama, G. Yu, K. L. Wong, N. Altieri, C. Grezes, N. Kioussis, *et al.*, *Applied Physics Letters* **110**, 052401 (2017).
- ³⁶ Y. Kato, H. Yoda, Y. Saito, S. Oikawa, K. Fujii, M. Yoshiki, K. Koi, H. Sugiyama, M. Ishikawa, T. Inokuchi, *et al.*, *Applied Physics Express* **11**, 053007 (2018).
- ³⁷ S. Kwon, Q. Sun, F. Mahfouzi, K. L. Wang, P. K. Amiri, and N. Kioussis, *Phys. Rev. Applied* **12**, 044075 (2019).
- ³⁸ S. Kwon, P.-V. Ong, Q. Sun, F. Mahfouzi, X. Li, K. L. Wang, Y. Kato, H. Yoda, P. K. Amiri, and N. Kioussis, *Physical Review B* **99**, 064434 (2019).
- ³⁹ T. Nozaki, M. Endo, M. Tsujikawa, T. Yamamoto, T. Nozaki, M. Konoto, H. Ohmori, Y. Higo, H. Kubota, A. Fukushima, *et al.*, *APL Materials* **8**, 011108 (2020).
- ⁴⁰ W. Z. Chen, L. N. Jiang, Z. R. Yan, Y. Zhu, C. H. Wan, and X. F. Han, *Phys. Rev. B* **101**, 144434 (2020).
- ⁴¹ S. Miwa, M. Suzuki, M. Tsujikawa, T. Nozaki, T. Nakamura, M. Shirai, S. Yuasa, and Y. Suzuki, *Journal of Physics D: Applied Physics* **52**, 063001 (2018).
- ⁴² K. L. Wang, H. Lee, and P. Khalili Amiri, *IEEE Transactions on Nanotechnology* **14**, 992 (2015).
- ⁴³ W. Kang, Y. Ran, Y. Zhang, W. Lv, and W. Zhao, *IEEE Transactions on Nanotechnology* **16**, 387 (2017).
- ⁴⁴ W. Kang, Y. Ran, W. Lv, Y. Zhang, and W. Zhao, *IEEE Magnetics Letters* **7**, 1 (2016).
- ⁴⁵ G. Zheng, S.-H. Ke, M. Miao, J. Kim, R. Ramesh, and N. Kioussis, *Scientific reports* **7**, 1 (2017).
- ⁴⁶ Y. Su, M. Li, J. Zhang, J. Hong, and L. You, *Journal of Magnetism and Magnetic Materials* **505**, 166758 (2020).
- ⁴⁷ P.-H. Chang, W. Fang, T. Ozaki, and K. Belashchenko, *arXiv preprint arXiv:2008.03249* (2020).
- ⁴⁸ J. Dijkstra, C. Van Bruggen, C. Haas, and R. de Groot, *Journal of Physics: Condensed Matter* **1**, 9163 (1989).
- ⁴⁹ T. Ito, H. Ido, and K. Motizuki, *Journal of Magnetism and Magnetic Materials* **310**, e558 (2007).
- ⁵⁰ L. Kahal, A. Zaoui, and M. Ferhat, *Journal of Applied Physics* **101**, 093912 (2007).
- ⁵¹ S. Polesya, G. Kuhn, S. Mankovsky, H. Ebert, M. Regus, and W. Bensch, *Journal of Physics: Condensed Matter* **24**, 036004 (2011).
- ⁵² W. Takei, D. E. Cox, and G. Shirane, *Physical Review* **129**, 2008 (1963).
- ⁵³ Q. L. He, X. Kou, A. J. Grutter, G. Yin, L. Pan, X. Che, Y. Liu, T. Nie, B. Zhang, S. M. Disseler, B. J. Kirby, W. Ratcliff II, Q. Shao, K. Murata, X. Zhu, G. Yu, Y. Fan, M. Montazeri, X. Han, J. A. Borchers, and K. L. Wang, *Nature Materials* **16**, 94 (2017).
- ⁵⁴ Q. L. He, G. Yin, L. Yu, A. J. Grutter, L. Pan, C.-Z. Chen, X. Che, G. Yu, B. Zhang, Q. Shao, A. L. Stern, B. Casas, J. Xia, X. Han, B. J. Kirby, R. K. Lake, K. T. Law, and K. L. Wang, *Phys. Rev. Lett.* **121**, 096802 (2018).
- ⁵⁵ T. Wang, D. Gao, and M. Si, *Japanese Journal of Applied Physics* **58**, 080910 (2019).
- ⁵⁶ G. Kresse and J. Hafner, *Physical Review B* **47**, 558 (1993).
- ⁵⁷ P. E. Blöchl, *Physical Review B* **50**, 17953 (1994).
- ⁵⁸ J. P. Perdew, K. Burke, and M. Ernzerhof, *Physical Review Letters* **77**, 3865 (1996).
- ⁵⁹ A. I. Snow, *Phys. Rev.* **85**, 365 (1952).
- ⁶⁰ G. Henkelman, A. Arnaldsson, and H. Jónsson, *Computational Materials Science* **36**, 354 (2006).
- ⁶¹ V. Wang, N. Xu, J. C. Liu, G. Tang, and W.-T. Geng, (2020), *arXiv:1908.08269*.
- ⁶² J. Neugebauer and M. Scheffler, *Physical Review B* **46**, 16067 (1992).
- ⁶³ G. Makov and M. Payne, *Physical Review B* **51**, 4014 (1995).
- ⁶⁴ G. Yu, Z. Wang, M. Abolfath-Beygi, C. He, X. Li, K. L. Wong, P. Nordeen, H. Wu, G. P. Carman, X. Han, I. A. Alhomoudi, P. K. Amiri, and K. L. Wang, *Applied Physics Letters* **106**, 072402 (2015).
- ⁶⁵ Z. Charifi, D. Guendouz, H. Baaziz, F. Soyalp, and B. Hamad, *Physica Scripta* **94**, 015701 (2018).
- ⁶⁶ D.-s. Wang, R. Wu, and A. J. Freeman, *Phys. Rev. B* **47**, 14932 (1993).
- ⁶⁷ See discussion surrounding Eq. (46) of N. Djavid and R. K. Lake, *Phys. Rev. B*, **102**, 024419 (2020).
- ⁶⁸ H. X. Yang, M. Chshiev, B. Dieny, J. H. Lee, A. Manchon, and K. H. Shin, *Phys. Rev. B* **84**, 054401 (2011).
- ⁶⁹ J. Okabayashi, J. W. Koo, H. Sukegawa, S. Mitani, Y. Takagi, and T. Yokoyama, *Applied Physics Letters* **105**, 122408 (2014).
- ⁷⁰ J. Towns, T. Cockerill, M. Dahan, I. Foster, K. Gauthier, A. Grimshaw, V. Hazlewood, S. Lathrop, D. Lifka, G. D. Peterson, *et al.*, *Computing in Science & Engineering* **16**, 62 (2014).